Exploring Subtropical Stratocumulus Multiple Equilibria Using a Mixed-Layer Model

ANDREA M. SALAZAR[a] AND ELI TZIPERMAN[a,b]

[a] *Department of Earth and Planetary Sciences, Harvard University, Cambridge, Massachusetts*
[b] *School of Engineering and Applied Sciences, Harvard University, Cambridge, Massachusetts*

ABSTRACT: Stratocumulus clouds cover about a fifth of Earth's surface, and due to their albedo and low-latitude location, they have a strong effect on Earth's radiation budget. Previous studies using large-eddy simulations have shown that multiple equilibria (both stratocumulus-covered and cloud-free/scattered cumulus states) exist as a function of fixed SST, with relevance to equatorward advected air masses. Multiple equilibria have also been found as a function of atmospheric CO_2, with a subtropical SST nearly 10 K higher in the cloud-free state and with suggested relevance to warm climate dynamics. In this study, we use a mixed-layer model with an added surface energy balance and the ability to simulate both the stratocumulus (coupled) and cloud-free/scattered cumulus (decoupled) states using a "stacked" mixed-layer approach to study both types of multiple equilibria and the corresponding hysteresis. The model's simplicity and computational efficiency allow us to qualitatively explore the mechanisms critical to the stratocumulus cloud instability and hysteresis as well as isolate key processes that allow for multiple equilibria via mechanism-denial experiments not possible with a full-complexity model. For the hysteresis in fixed SST, we find that decoupling can occur due to either enhanced entrainment warming or a reduction in cloud-top longwave cooling. The critical SST at which decoupling occurs is highly sensitive to precipitation and entrainment parameterizations. In the CO_2 hysteresis, decoupling occurs in the simple model used even without the inclusion of SST–cloud cover feedbacks, and the width of the hysteresis displays the same sensitivities as the fixed SST case. Overall, the simple model analysis and results motivate further studies using higher complexity models.

KEYWORDS: Stratiform clouds; Cloud cover; Cloud radiative effects

1. Introduction

Stratocumulus clouds are low-altitude clouds that form beneath sharp temperature inversions, where convection between the surface and the cloud layer is driven by cloud-top longwave cooling (Turton and Nicholls 1987; Bretherton and Wyant 1997; Wood 2012). On an annual average, stratocumulus clouds cover about 20% of Earth's surface and are particularly concentrated over subtropical eastern ocean margins (Warren et al. 1988; Hahn and Warren 2007). Their location, combined with their prevalence and high albedo, means that they have a considerable effect on Earth's radiation budget, providing a net local forcing of up to -100 W m^{-2} in subtropical regions (Klein and Hartmann 1993; Loeb et al. 2018).

Cloud-top longwave cooling causes turbulent convective motions that homogenize the boundary layer and couple surface moisture fluxes to the cloud layer. These fluxes sustain the cloud layer against strong entrainment warming and drying through mixing with the troposphere across the inversion layer (Lilly 1968; Nicholls 1984; Bretherton and Wyant 1997). Turbulence is also enhanced by latent heat fluxes from the surface and latent heat release within the cloud layer (Bretherton and Wyant 1997; Zheng et al. 2018). Convection between the surface and cloud layer is interrupted when cloud-top longwave cooling weakens (Lilly 1968; Tan et al. 2017), when entrainment warming becomes too strong (Bretherton and Wyant 1997; van der Dussen et al. 2014), or when enhanced subcloud evaporation of

precipitation stabilizes the boundary layer (Turton and Nicholls 1987; Rapp 2016). Under these conditions, the cloud layer is effectively cut off (decoupled) from its surface moisture supply. Though in some cases, a decoupled boundary layer can allow a stratocumulus deck to persist with cumulus clouds beneath (Pedruzo-Bagazgoitia et al. 2020; Zouzoua et al. 2021), in this work, we will focus on the case where stratocumulus clouds give way to either much less reflective scattered cumulus clouds or no clouds. The decrease in albedo associated with this cloud transition can cause considerable surface warming (Schneider et al. 2019).

Bellon and Geoffroy (2016) found a hysteresis in stratocumulus cloud cover as a function of fixed SST using a large-eddy simulation (LES), where multiple equilibria (i.e., both cloudy and noncloudy states) are possible between SST values of 288 and 294 K. The presence of multiple equilibria was attributed to the cloud radiative effect, in which a cloud-free or scattered cumulus-topped (decoupled) layer would have a low emissivity and weak longwave cooling while a stratocumulus-topped (coupled) layer would have a high emissivity and strong longwave cooling. The demise of the stratocumulus equilibrium with increased SST was attributed to an enhancement of entrainment drying across the inversion layer above the cloud. The enhanced entrainment is driven at high prescribed SST by turbulence produced by increased latent heat fluxes from the surface. This enhanced entrainment drying leads to a lower liquid water path (LWP) in the cloud layer and therefore weaker longwave cooling at the cloud top. This fixed SST scenario ignores the cloud cover–SST feedback.

More recent work has investigated how stratocumulus cloud cover in the presence of an interactive SST can change

---

due to CO_2-driven climate warming and experience bistability and hysteresis. Schneider et al. (2019) analyzed a hysteresis of stratocumulus clouds as a function of atmospheric CO_2. For CO_2 values between ∼300 and ∼1200 ppm, both stratocumulus-covered (coupled) and scattered cumulus (decoupled) states were possible. They attributed the breakup of the stratocumulus equilibrium at high CO_2 to the increased opacity of the free troposphere due to a higher CO_2 concentration as well as a higher water vapor mixing ratio due to increased temperature in the free troposphere, which increases the downwelling longwave radiation (the water vapor feedback) and therefore weakens the net longwave cooling at the cloud top, ceasing convection. As the CO_2 is then decreased, it needs to be lowered to CO_2 values smaller than the original critical CO_2 value in order to regain the coupled equilibrium. The abrupt breakup of the cloud layer due to rising CO_2 levels may be relevant to future climate change as well as to past periods of hothouse climates such as the Eocene (56–48 Myr; Schneider et al. 2019). This adds to previous work on cloud feedbacks in warm climates, including a possible role for polar stratospheric clouds (Sloan and Pollard 1998; Kirk-Davidoff et al. 2002), a convective Arctic cloud feedback that can lead to multiple equilibria and keep the arctic ocean ice free (Abbot and Tziperman 2008b, 2009), and low clouds over land due to the advection of moist air from the ocean, which can prevent the surface from reaching subfreezing temperatures during wintertime (Cronin and Tziperman 2015).

Stratocumulus-topped boundary layers (STBLs) have been studied with multiple models, ranging from simple mixed-layer models (MLM; Lilly 1968; Turton and Nicholls 1987; Bretherton and Wyant 1997; Pelly and Belcher 2001) to LES (Uchida et al. 2010; Bretherton and Wyant 1997; Bellon and Geoffroy 2016; Schneider et al. 2019; Matheou and Teixeira 2019). Simple models have not been used to investigate the hysteresis behavior found in LES as a function of SST or CO_2 (Bellon and Geoffroy 2016; Schneider et al. 2019) because the assumption of a well-mixed boundary layer breaks down when the layer decouples from the surface. However, the diurnal cycle of stratocumulus clouds was studied by Turton and Nicholls (1987), who used a "stacked" mixed-layer approach to model decoupled solutions.

Our objective is to explore the processes behind the multiple equilibria and hysteresis behavior of stratocumulus cloud layers first as a function of CO_2 and then as a function of SST. The general motivation is to understand the role of such cloud feedbacks in warm climates. Our goal is to explore (i) what nonlinearities specifically allow for multiple equilibria in each case and (ii) what factors influence the critical SST or CO_2 at which the cloud layer onset or breakup occurs. By performing a suite of mechanism-denial experiments and sensitivity tests using a mixed-layer model, we are able to qualitatively explore the physics and parameters that control the hysteresis behavior. For this purpose, we adapt a mixed-layer model to include a surface energy balance and the ability to model decoupled solutions through a stacked mixed-layer approach following Turton and Nicholls (1987). We validate the model by reproducing the instability that causes a breakup of stratocumulus clouds with increasing SST following Bellon and Geoffroy (2016) and in CO_2 based on Schneider et al. (2019).

Both of these previous studies were performed using LES, whose high computational expense and difficulty in selectively turning off different physics components prevented a thorough investigation of the mechanisms controlling the hysteresis. We, therefore, utilize the simplicity of our model to qualitatively study the fundamental mechanisms of the hysteresis in CO_2 and SST.

We find that for the CO_2 hysteresis, SST–cloud cover feedbacks and the water vapor feedback are not essential for decoupling (and therefore hysteresis) to occur in this model, unlike what was hypothesized by Schneider et al. (2019). We also find that decoupling with increasing CO_2 is due only to a weakening of longwave cooling as in Schneider et al. (2019). However, for the fixed SST hysteresis, we find that decoupling can occur either due to an enhancement of entrainment warming, as proposed by Bellon and Geoffroy (2016), but also due to a weakening of cloud-top longwave cooling. In both cases, the presence of multiple equilibria is attributed to the nonlinear dependence of cloud emissivity on the cloud liquid water path. Additionally, both hystereses show strong sensitivity to processes such as precipitation and entrainment, both of which are heavily influenced by cloud microphysics, a sensitivity of the hysteresis behavior that has not been explored in previous studies.

In section 2, we describe the modified MLM that includes a surface energy balance and allows decoupled solutions. This model is then used to explore the dynamics of multiple equilibria and hysteresis in CO_2 and fixed SST in section 3. We conclude in section 4.

2. Model description

In this section, we describe the mixed-layer model, including the interactive ocean mixed-layer component. We assume that moist static energy, $\mathrm{MSE} = c_p T + Lq_v + gz$, and total (vapor plus liquid) specific humidity, $q_t = q_v + q_l$, are well mixed throughout the layer in the coupled state and are therefore constant in height (Lilly 1968). Here, c_p is the specific heat of air, T is the temperature at altitude z, L is the latent heat of vaporization for water vapor, and g is the acceleration due to gravity. In section 2a, we describe the coupled mixed-layer model equations that follow Bretherton and Wyant (1997), with a surface energy balance added. In section 2c, we follow Turton and Nicholls (1987) and model-decoupled solutions by stacking a "surface mixed layer" beneath the "decoupled mixed layer." The difference in the vertical structure of conserved variables between the coupled and decoupled state is summarized in Fig. 1.

a. Modeling the coupled state

As in Lilly (1968) and Bretherton and Wyant (1997), the prognostic equations for moist static energy in the mixed layer MSE_M and total specific humidity in the mixed layer q_{tM} are

$$\frac{d\mathrm{MSE}_M}{dt} = -\frac{\partial E}{\partial z} = -\frac{\partial}{\partial z}(\langle w'\mathrm{MSE}'\rangle + F_R/\rho_a), \quad (1)$$

$$\frac{dq_{tM}}{dt} = -\frac{\partial W}{\partial z} = -\frac{\partial}{\partial z}(\langle w'q'_{tM}\rangle - F_P), \quad (2)$$
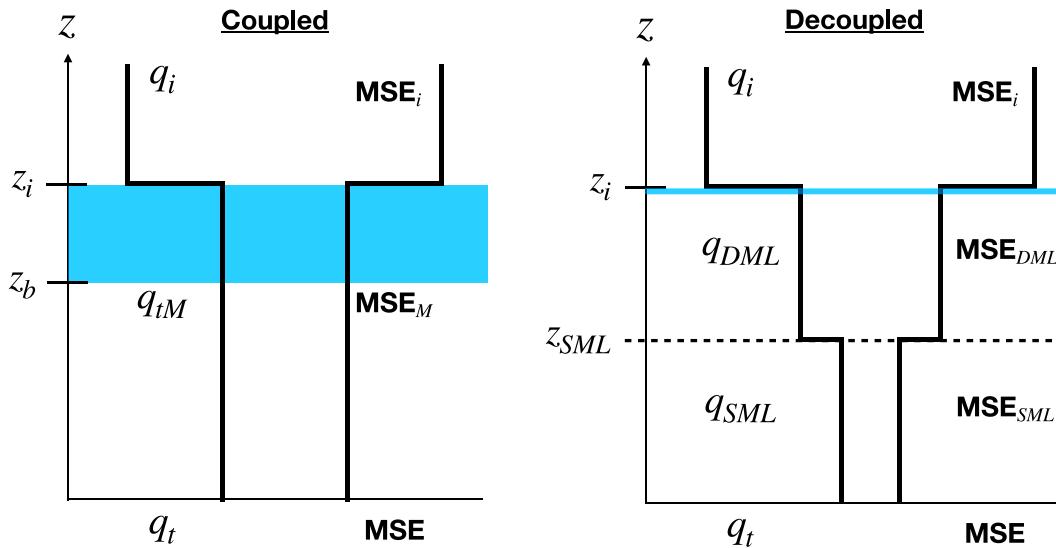
FIG. 1. Vertical profiles of total (vapor plus liquid) specific humidity q_t and MSE in both the coupled and decoupled states. The blue patch represents the cloud layer within the mixed layer, which is infinitely thin when the layer is decoupled.

where E and W are the total energy and moisture vertical fluxes and ρ_a is the density of air. Angle brackets indicate horizontally averaged fluxes and F_R (W m^{-2}) and F_P (kg kg^{-1} m s^{-1}) are the net upward radiative flux and the precipitation flux, respectively. The conservation equations for the full mixed layer are found by integrating Eqs. (1) and (2) from the surface to the top of the layer z_i.

In order for the MSE and total specific humidity in the mixed layer to remain vertically uniform, the energy and moisture flux convergences appearing in the above equation must be independent of height, and therefore the corresponding fluxes must be linear functions of height:

$$E(z) = \left(1 - \frac{z}{z_i}\right)E(0) + \frac{z}{z_i}E(z_i), \qquad (3)$$

$$W(z) = \left(1 - \frac{z}{z_i}\right)W(0) + \frac{z}{z_i}W(z_i). \qquad (4)$$

Surface fluxes, defined at $z = 0$, are calculated using bulk aerodynamic formulas:

$$E(0) = C_T V(\text{MSE}_s - \text{MSE}_M) + F_R(0)/\rho_a, \qquad (5)$$

$$W(0) = C_T V(q_s - q_{tM}) - F_P(0), \qquad (6)$$

where MSE_s and q_s are the saturation surface moist energy and specific humidity, and C_T and V are the transport parameter and the 10-m wind speed, respectively. At the surface, $F_R(0)$ is the net upward radiation, and $F_P(0)$ is the precipitation that reaches the surface. At the inversion just above the mixed layer, entrainment mixing leads to energy and moisture fluxes of the form:

$$E(z_i) = -w_e^{\text{inv}}(\text{MSE}_i - \text{MSE}_M) + F_R(z_i)/\rho_a, \qquad (7)$$

$$W(z_i) = -w_e^{\text{inv}}(q_i - q_{tM}), \qquad (8)$$

where MSE_i and q_i are the moist static energy and specific humidity just above the cloud layer. We assume the warm air above the cloud layer originates from updrafts in the tropics and will therefore warm with increasing CO_2 levels (Schneider et al. 2019), assuming a tropical climate sensitivity of 3°C. For our radiation calculation, we assume that the troposphere above the cloud layer is isothermal with constant relative humidity RH_i. The temperature of the troposphere above the cloud layer is prescribed as a function of CO_2 and inversion height z_i:

$$T_i = T_{io} + 3 \log_2\left(\frac{CO_2}{280}\right) - \Gamma_i(z_i - z_{io}). \qquad (9)$$

We choose T_{io} to roughly match the temperature just above the inversion layer for stratocumulus-topped boundary layers (Nicholls 1984). The value of z_{io} is calculated in the model when CO_2 is 280 ppm. The lapse rate above the cloud layer Γ_i is assumed to follow a moist adiabat (Table 1). Using a constant relative humidity in the troposphere above the cloud layer RH_i the specific humidity in the troposphere q_i can be calculated from the Clausius–Clapeyron relationship. As the layer is assumed isothermal and the relative humidity is fixed in space and time, q_i is assumed independent of height within the troposphere.

Using a form similar to Pelly and Belcher (2001), we define the entrainment rate w_e^{inv} of warm, dry air from the troposphere into the cloud layer as

$$\rho_a c_p w_e^{\text{inv}} = \begin{cases} C\dfrac{\Delta F_R - \mu L \Delta F_p}{\Delta \theta_v^{i-c}} & \text{coupled} \\[2ex] \rho_a c_p w_{\text{ed}}^{\text{inv}} & \text{decoupled} \end{cases}, \qquad (10)$$

TABLE 1. Table of constants in the order of appearance in the text. References include 1) Schneider et al. (2019), 2) Bretherton and Wyant (1997), and 3) Turton and Nicholls (1987). An asterisk indicates a parameter that was tuned to give the best agreement with the CO_2 hysteresis in Schneider et al. (2019).

Variable	Value	Description
c_p	1005.7 J kg^{-1} K^{-1}	Specific heat of air
L	2.25×10^6 J kg^{-1}	Latent heat of vaporization
g	9.8 m s^{-2}	Acceleration due to gravity
ρ_a	1.225 kg m^{-3}	Air density
C_T	0.001 (1 + 0.07V)	Transport parameter (2)
V	7.1 m s^{-1}	10-m wind speed (2)
T_{io}	290 K	Initial inversion temperature*
Γ_i	6.5 K km^{-1}	Lapse rate in free troposphere
RH_i	0.4	Relative humidity of free troposphere*
z_{io}	915 m	Inversion height at 280 ppm
C	0.5	Entrainment efficiency*
μ	0.93	Thermodynamic factor [Eqs. (10) and (28)] (2)
T_{ref}	273 K	Reference temperature
w_{ed}^{inv}	0.0056 m s^{-1}	Decoupled cloud-top entrainment rate, CO_2 hysteresis* (3)
w_{ed}^{inv}	0.002 m s^{-1}	Decoupled cloud-top entrainment rate, SST hysteresis
τ_{precip}	0.7 h	Precipitation time scale*
Γ_p	0.86×10^{-5} kg kg^{-1} km^{-1}	Evaporation rate beneath cloud base (3)
τ_{export}	3.96 years	Moisture export time scale (1)
ϵ_{co}	0.45	Minimum cloud layer emissivity
D_c	1.66	Diffusivity factor
κ	90.36 m^2 kg^{-1}	Absorption coefficient of water droplets
A	0.05	Climate sensitivity to CO_2
B	0.1	Climate sensitivity to H_2O
σ	5.67×10^{-8} W m^{-2} K^{-4}	Stefan–Boltzmann constant
ϵ_{io}	0.5	Minimum free troposphere emissivity
D	6×10^{-6} s^{-1}	Large-scale divergence (1)
p_o	1000 hPa	Surface pressure
S	471 W m^{-2}	Diurnally averaged insolation (1)
OHU	10 W m^{-2}	Ocean heat uptake*
α_w	0.06	Albedo of water
α_c	0.6	Maximum albedo of cloud
s_{vo}/c_p	300 K	Reference virtual static energy
w_e^{SML}	0.013 m s^{-1}	Entrainment in SML, CO_2 hysteresis*
w_e^{SML}	0.003 m s^{-1}	Entrainment in SML, SST hysteresis
q_{to}^{DML}	8 g kg^{-1}	Initial DML total moisture, CO_2 hysteresis
q_{to}^{DML}	3.5 g kg^{-1}	Initial DML total moisture, SST hysteresis
z_{SML}	200 m	SML top height
z_{id}	1000 m	Decoupled inversion height

where C is a prescribed constant entrainment efficiency, ΔF_R is the net longwave cooling by the cloud layer, ΔF_P is the net precipitation flux across the mixed layer, $\mu = (1 - \delta c_p T_{ref}/L)$, and $\Delta \theta_v^{i-c}$ is the jump in virtual potential temperature across the inversion. We define virtual potential temperature as $\theta_v = \theta(1 + \delta q_v - q_l)$, where $\delta = (R_v/R_d) - 1$, θ is potential temperature, and R_v and R_d are the gas constants for water vapor and dry air, respectively. Entrainment is driven by convective turbulence in the mixed layer and is inhibited by a stable stratification across the cloud top. Therefore, sources and sinks of turbulence (net longwave cooling and evaporative cooling of drizzle beneath the cloud base) appear in the numerator of Eq. (10), and the inversion strength is in the denominator. This parameterization is very similar to the energy balance entrainment rate described in Bretherton and Wyant (1997) and the "minimum entrainment" closure by Lilly (1968). When the cloud

layer is decoupled from the surface, we set the entrainment to a background value w_{ed}^{inv} to avoid numerical instabilities that arise from very small $\Delta \theta_v^{i-c}$ in a decoupled state. This value is loosely constrained by the cloud-top entrainment rates in the decoupled state in Turton and Nicholls (1987).

The precipitation flux F_P is assumed constant throughout the cloud and decreases linearly with height beneath the cloud base at a rate of Γ_P, as in Turton and Nicholls (1987). By defining a constant time scale of precipitation τ_{precip}, we write the precipitation flux as a function of height z and cloud LWP:

$$F_p(z) = \begin{cases} \dfrac{LWP}{\rho_a \tau_{precip}} & z_i > z \geq z_b \\ \dfrac{LWP}{\rho_a \tau_{precip}} - \Gamma_p(z_b - z) & z < z_b, \end{cases} \quad (11)$$
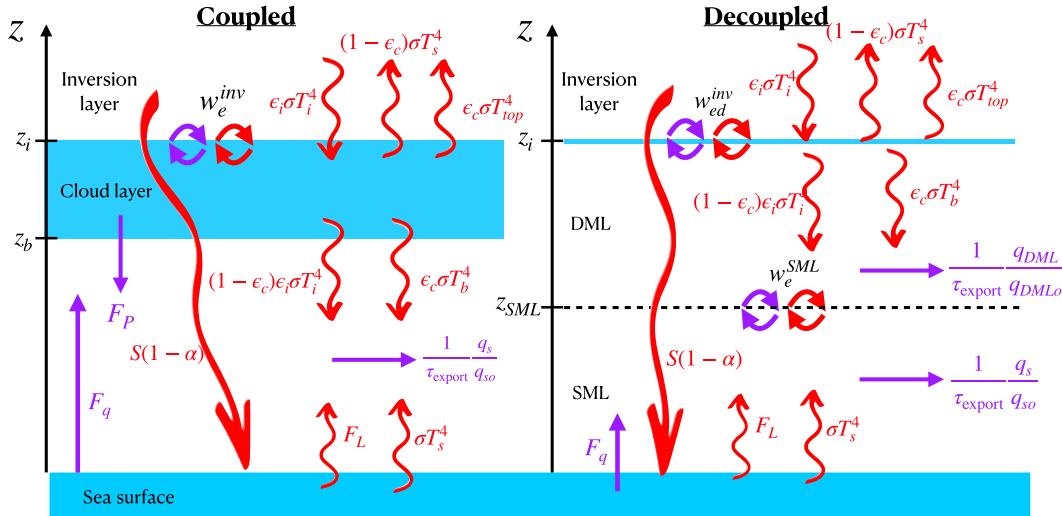
FIG. 2. A schematic of the fluxes in the mixed-layer model where red arrows correspond to terms in the energy budgets for the surface and mixed layer(s). Purple arrows correspond to terms in the moisture budget. When the model is decoupled, the cloud layer is infinitely thin, and there is no precipitation.

where z_b is the cloud-base height, defined as the altitude where saturation is reached. The cloud liquid water path is defined as the integrated liquid water specific humidity throughout the cloud layer:

$$\text{LWP} = \int_{z_b}^{z_i} \rho_a q_l \, dz = \frac{\rho_a q_l^{\text{top}}}{2}(z_i - z_b), \tag{12}$$

where the integral was evaluated by noting that the liquid water specific humidity q_l increases linearly through the cloud layer (Bretherton and Wyant 1997). The liquid water specific humidity at the top of the cloud q_l^{top} is found by constructing vertical profiles of temperature and q_l through the mixed layer using MSE_M and $q_{tM} = q_v + q_l$ and assuming q_v is the saturation specific humidity throughout the cloud.

Combining Eqs. (1)–(8), we write the time evolution equations of MSE_M and q_{tM} as

$$z_i \frac{d\text{MSE}_M}{dt} = C_T V(\text{MSE}_s - \text{MSE}_M) + w_e^{\text{inv}}(\text{MSE}_i - \text{MSE}_M)$$
$$- \Delta F_R/\rho_a, \tag{13}$$

$$z_i \frac{dq_{tM}}{dt} = C_T V(q_s - q_{tM}) - w_e^{\text{inv}}(q_{tM} - q_i) - \Delta F_P - z_i \frac{q_s}{q_{so}} \frac{1}{\tau_{\text{export}}}. \tag{14}$$

The last term contains an added moisture export out of the subtropics and into other regions of the form used in Schneider et al. (2019) that scales with the saturation specific humidity at the surface q_s and has a constant time scale of export τ_{export} directly taken from Schneider et al. (2019). In the coupled case, this term is small compared to the other moisture budget terms, but it becomes more important in the decoupled case when other terms are small.

The net longwave cooling across the layer ΔF_R is the difference in the net upward longwave flux between the cloud top and the surface. Since there is no precipitation flux entering from above at the cloud top, the net precipitation flux across the layer is simply the precipitation flux at the surface $F_P(0)$. We use a simple radiation parameterization, illustrated in Fig. 2, rather than the two-stream approximation used by Bretherton and Wyant (1997). At the cloud top, the net upward longwave radiation is

$$F_R(z_i) = \epsilon_c \sigma T_{\text{top}}^4 + (1 - \epsilon_c)\sigma T_s^4 - \epsilon_i \sigma T_i^4, \tag{15}$$

where T_{top} is the temperature of the cloud top, found by making vertical profiles of temperature using the MSE_M and q_{tM}, and T_s is the sea surface temperature, calculated from Eq. (21). The emissivity of the cloud ϵ_c is found as a function of LWP by assuming the cloud acts as a graybody:

$$\epsilon_c = 1 - (1 - \epsilon_{co})\exp(-D_c \kappa \text{LWP}), \tag{16}$$

where D_c is a nondimensional diffusivity factor, and κ is the absorption coefficient of liquid water (Neale et al. 2010). In the absence of liquid water (no cloud), the emissivity is set to a minimum value ϵ_{co} due to the CO_2 and water vapor in the mixed layer.

As described in Eq. (9), we assume that the troposphere above the cloud layer is isothermal with temperature T_i, which depends on the CO_2 value and on the altitude of the inversion z_i. Similar to Sasamori (1968), the emissivity of the troposphere is written as a function of CO_2 and q_i:

$$\epsilon_i = \epsilon_{io} + A \log_2\left(\frac{CO_2}{280}\right) + B \log_2\left(\frac{q_i}{q_{io}}\right), \tag{17}$$

where A is tuned by running the full MLM model to give a surface warming of 1.5°C for a doubling of CO_2 when $B = 0$.

The value of B is tuned to give a surface warming of 3°C for a doubling of CO_2 when including the water vapor feedback.

At the surface, the net upward radiation is

$$F_R(0) = \sigma T_s^4 - \epsilon_c \sigma T_b^4 - (1 - \epsilon_c)\epsilon_i \sigma T_i^4, \qquad (18)$$

where T_b is the temperature at the base of the cloud. Combining Eqs. (15) and (18), the net longwave cooling across the mixed layer is

$$\Delta F_R = \epsilon_c \sigma(T_{\text{top}}^4 + T_b^4) - \epsilon_c \sigma T_s^4 - \epsilon_c \epsilon_i \sigma T_i^4. \qquad (19)$$

Finally, we write the mass continuity equation for the boundary layer as well as the added surface energy balance:

$$\frac{dz_i}{dt} = w_e^{\text{inv}} - Dz_i, \qquad (20)$$

$$C_s \frac{dT_s}{dt} = S(1 - \alpha) + \epsilon_c \sigma T_b^4 + (1 - \epsilon_c)\epsilon_i \sigma T_i^4 - \sigma T_s^4$$
$$- \rho_a C_T V(\text{MSE}_s - \text{MSE}_M) - \text{OHU}, \qquad (21)$$

where S is the diurnally averaged insolation in June in the subtropics (neglecting tropospheric absorption), D is the large-scale divergence, and α is the albedo of the cloud layer:

$$\alpha = \alpha_c - (\alpha_c - \alpha_w)\exp(-D_c \kappa \text{LWP}), \qquad (22)$$

a form qualitatively consistent with Gettelman (2015). We set a maximum cloud albedo α_c and a minimum albedo representing the reflectivity of the sea surface α_w. The second to last term in the surface energy budget Eq. (21) is a combination of sensible and latent heat fluxes and the last term OHU represents ocean heat uptake (Table 1).

The model requires the calculation of the cloud-base height z_b as well as the temperature at the cloud base T_b. These may be determined by solving for z_b and T_b from the moist static energy $\text{MSE}_M(z_b) = c_p T_b + L q_{tM} + g z_b$ and from the condition that saturation is reached at the cloud base z_b, $q_{tM} = q^*(z_b, T_b)$, where q^* is the saturation specific humidity. If z_b is greater than z_i (as in the decoupled, dry case in this model), we set the cloud base equal to the cloud top to represent an infinitely thin cloud layer. At the cloud top, the specific humidity may be smaller than the total moisture q_{tM} when liquid water exists, and we similarly solve for the temperature at the cloud top T_{top} from the moist static energy, $\text{MSE}_M(z_i) = c_p T_{\text{top}} + L \min[q_{tM}, q^*(z_i, T_{\text{top}})] + g z_i$, where z_i is calculated using Eq. (20).

b. Diagnosing decoupling

To begin, we solve the set of Eqs. (13), (14), (20), and (21) for the steady-state values of MSE_M, q_{tM}, z_i, and T_s by setting the time derivatives to zero and using a root solver (fsolve in SciPy). When a stratocumulus cloud layer is coupled to the surface, kinetic energy is primarily produced within the cloud layer by longwave cooling and entrainment drying, which cools parcels such that they are negatively buoyant and sink through the mixed layer and to the surface. Decoupling occurs when negative buoyancy fluxes (downward motion of light parcels) convert turbulent kinetic energy to potential energy. The weaker turbulence weakens the convective motions and inhibits the parcel from reaching the surface (Bretherton 1997), creating two distinct layers with a stably stratified transition layer between them.

Following Bretherton and Wyant (1997), we write the vertical structure of the buoyancy flux as

$$\langle w'b' \rangle(z) = (g/s_{vo})\langle w's_v' \rangle(z), \qquad (23)$$

where s_{vo} is a reference virtual static energy (see Table 1), and s_v is the virtual static energy (equivalent to virtual potential temperature, a proxy for buoyancy):

$$s_v = c_p[T + T_{\text{ref}}(\delta q_v - q_l)] + gz,$$

where $\delta = (R_v/R_d) - 1 \approx 0.61$. To obtain a profile of the buoyancy flux with height, we must write the virtual static energy in terms of known variables (MSE_M and q_{tM}):

$$s_v = \text{MSE}_M - q_v L\left(1 - \frac{\delta c_p T_{\text{ref}}}{L}\right) - c_p T_{\text{ref}} q_l. \qquad (24)$$

Decoupling occurs when there are negative buoyancy fluxes beneath the cloud base. The lack of liquid water beneath the cloud implies $q_l = 0$ there. Using the definition $q_{tM} = q_v + q_l$, this allows us to write $q_v = q_{tM}$ beneath the cloud. Defining $\mu = (1 - \delta c_p T_{\text{ref}}/L)$,

$$s_v(z < z_b) = \text{MSE}_M - \mu L q_{tM}, \qquad (25)$$

$$\langle w's_v' \rangle(z < z_b) = \langle w'\text{MSE}_M' \rangle - \mu L \langle w'q_{tM}' \rangle. \qquad (26)$$

Equation (26) gives the subcloud buoyancy flux in terms of fluxes of the known variables in the model. Rearranging Eqs. (3)–(8), the subcloud buoyancy flux can be written as

$$\langle w's_v \rangle(z = z_b) = \overbrace{\left(1 - \frac{z_b}{z_i}\right)C_T V(\text{MSE}_s - \text{MSE}_M)}^{\text{Convective heat flux}} + \overbrace{\frac{z_b}{z_i}\Delta F_R/\rho_a}^{\text{Net longwave cooling}}$$

$$- \overbrace{\frac{z_b}{z_i}w_e^{\text{inv}}(\text{MSE}_i - \text{MSE}_M) + \frac{z_b}{z_i}\mu L w_e^{\text{inv}}(q_i - q_{tM})}^{\text{Entrainment warming and drying}}$$

$$- \underbrace{\left(1 - \frac{z_b}{z_i}\right)C_T V L(q_s - q_{tM})}_{\text{Latent heat flux}} - \underbrace{\mu L\left[F_p(z_b) - \left(1 - \frac{z_b}{z_i}\right)\Delta F_p\right]}_{\text{Subcloud drizzle evaporative cooling}} \qquad (27)$$

We invoke a strict decoupling criterion, similar to the minimal decoupling criterion in Bretherton and Wyant (1997), such that if there are negative buoyancy fluxes beneath the cloud, the mixed layer decouples:

$$\langle w's'_v \rangle (z = z_b) \begin{cases} \geq 0 & \text{coupled} \\ < 0 & \text{decoupled} \end{cases}. \quad (28)$$

Looking at individual terms in the vertical flux profile, we can learn about the physical processes that can lead to decoupling. For example, net longwave cooling is a source of positive buoyancy flux and therefore a producer of turbulent kinetic energy (TKE). The convective heat flux at the cloud base also provides TKE by encouraging mixing. Evaporation of drizzle beneath the cloud destroys TKE by working to stabilize the stratification there. Cloud-top entrainment warming combats the evaporative cooling due to entrainment drying and also destroys TKE. The competition of all of these terms determines the total subcloud buoyancy flux.

We check the decoupling criterion after finding the steady states of Eqs. (13), (14), (20), and (21). If it is positive, the mixed layer is coupled, and the solution is accepted as physical. If the decoupling criterion is negative, the mixed layer is decoupled, and the well-mixed assumption is no longer valid, so we transition to the stacked mixed-layer model described below.

c. Decoupled model

In Fig. 1, we show the model configuration for a decoupled state. Instead of a single well-mixed layer, the model is split into two stacked mixed layers, a surface mixed layer (SML) and a decoupled mixed layer (DML), following Turton and Nicholls (1987). The DML is isolated from direct surface fluxes and receives surface moisture and energy only through mixing with the SML. Each mixed layer has its own energy and moisture budgets, similar to Eqs. (13) and (14).

The SML is coupled to the surface and experiences mixing at the top with the DML:

$$z_{SML} \frac{dMSE_{SML}}{dt} = C_T V(MSE_s - MSE_{SML})$$
$$+ w_e^{SML}(MSE_{DML} - MSE_{SML}), \quad (29)$$

$$z_{SML} \frac{dq_{SML}}{dt} = C_T V(q_s - q_{SML}) - w_e^{SML}(q_{SML} - q_{DML})$$
$$- z_{SML} \frac{q_s}{q_{so}} \frac{1}{\tau_{export}}, \quad (30)$$

where w_e^{SML} is the entrainment rate between the SML and the DML, set as a constant in this model (see Table 1). We assume a constant thickness of the SML z_{SML}. Note that we also include the moisture export term out of the SML as in the coupled state.

The energy and moisture budgets for the DML are

$$(z_{id} - z_{SML}) \frac{dMSE_{DML}}{dt} = w_e^{inv}(MSE_i - MSE_{DML})$$
$$- w_e^{SML}(MSE_{DML} - MSE_{SML}) - \Delta F_R / \rho_a, \quad (31)$$

$$(z_{id} - z_{SML}) \frac{dq_{DML}}{dt} = w_e^{SML}(q_{SML} - q_{DML}) - w_e^{inv}(q_{DML} - q_i)$$
$$- (z_i - z_{SML}) \frac{q_{DML}}{q_{DMLo}} \frac{1}{\tau_{export}} - \Delta F_P, \quad (32)$$

where z_{id} is the DML top height, set as a constant in a decoupled case, and $z_{id} - z_{SML}$ is the thickness of the DML. The precipitation flux ΔF_P is calculated as in Eq. (11), although we note that in all the results shown in this paper there is no liquid water in the DML for all the results, so the precipitation flux is calculated to be zero. The lack of liquid water in the DML is a result of the model equations and is not enforced directly. In general, a nonzero LWP in the DML corresponding to a "scattered cumulus" regime may arise by enhanced mixing with the SML or due to a weaker moisture export. We also note that the prescription of constant entrainment rates and layer thicknesses in the SML and DML is a simplification of the treatment of Turton and Nicholls (1987). These assumptions were made to model the decoupled state in the simplest way possible, while still allowing us to explore the qualitative behavior of stratocumulus instabilities, multiple equilibria, and hysteresis. These assumptions are justified after the fact by the ability of the model to simulate both hystereses with respect to CO_2 and SST.

When the mixed layer is decoupled from the surface, there is a stable stratification layer between the SML and DML, which inhibits the surface moisture and heat fluxes from reaching the DML. In other words, the stratification

$$\Delta \theta_v = \theta_v^{SML} - \theta_v^{DML} > 0. \quad (33)$$

After finding the steady states of Eqs. (31) and (32), we check the sign of $\Delta \theta_v$, and if it is positive, the mixed layer is decoupled. Following Turton and Nicholls (1987), when $\Delta \theta_v \leq 0$, the mixed layer recouples and Eqs. (13) and (14) are used.

The surface energy balance is nearly identical to Eq. (21), except now sensible and latent heat fluxes are calculated between the surface and the SML:

$$C_s \frac{dT_s}{dt} = S(1 - \alpha) + \epsilon_c \sigma T_b^4 + (1 - \epsilon_c)\epsilon_i \sigma T_i^4 - \sigma T_s^4$$
$$- \rho_a C_T V(MSE_s - MSE_{SML}) - OHU. \quad (34)$$

Several parameters in the model were tuned to give the best agreement with Schneider et al. (2019) of quantities such as the width of the hysteresis (the range of CO_2 or SST values in which multiple equilibria exist), the latent heat release from the surface, the cloud LWP, etc. The entrainment efficiency C was tuned be in the range reported by Pelly and Belcher (2001). The range of precipitation time scales τ_{precip} is roughly motivated by observations of drizzle beneath stratocumulus-topped boundary layers. The constant entrainment rates in the decoupled case w_e^{SML} and w_{ed}^{inv} were tuned based on the corresponding entrainment rates in Turton and Nicholls (1987). Our results as well as the sensitivity of our results to all of these parameters are given in section 3.
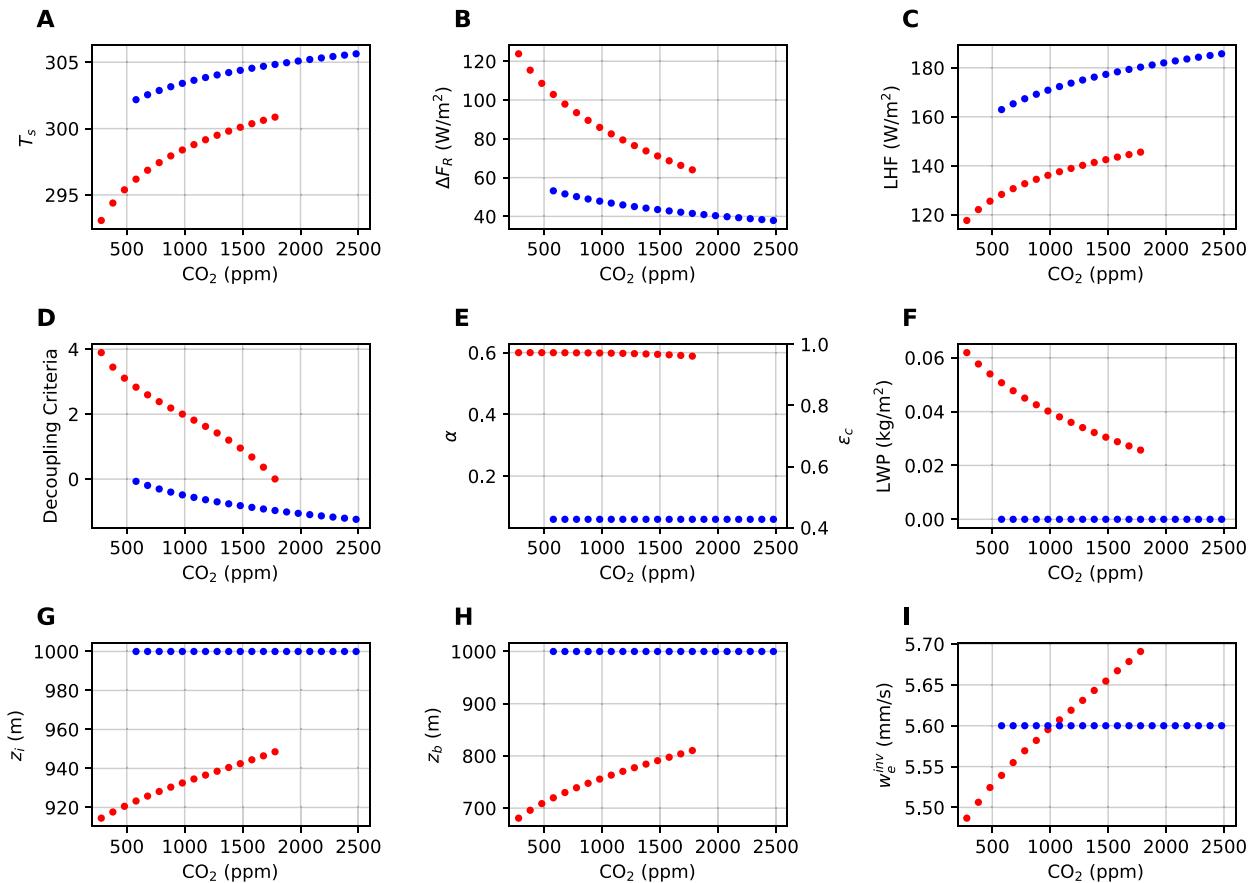
FIG. 3. Hysteresis in CO_2. Red dots indicate coupled solutions while blue dots indicate decoupled solutions. (a) SST (T_s). (b) Net long-wave cooling across the mixed layer [Eq. (19)]. (c) Surface latent heat flux. (d) Decoupling/coupling criteria [Eq. (28) for coupled solutions and the negative of Eq. (33) for decoupled solutions]. Note that the coupled solutions have been scaled up for plotting purposes. (e) Total albedo, including cloud and surface, and cloud emissivity. (f) Cloud liquid water path. (g) Height of mixed-layer top (inversion height, z_i). (h) Cloud-base height, where in the decoupled case when there is no cloud the cloud base is equal to the cloud top. (i) Cloud-top entrainment rate.

To construct the hysteresis, we first solve for the steady states of Eqs. (13), (14), (20), and (21) by setting the time derivatives to zero and using a root solver (fsolve in SciPy). We then check the decoupling criterion [Eq. (28)], and if it is negative, we deduce that the mixed layer is decoupled, and we solve Eqs. (29)–(32) to obtain the steady state of q_{DML}, MSE_{DML}, and T_s. To find and calculate multiple equilibria when they exist, for each CO_2 value we provide many initial guesses to the root solver and sort the solutions into coupled and decoupled equilibria by checking the decoupling criterion.

3. Results

In this section, we present and analyze the results of the mixed-layer model for bistability first as a function of CO_2 (section 3a) and then as a function of prescribed SST (section 3b). For each case, we explore the sensitivity of the width of the hysteresis to various model parameters and determine the minimum (lowest complexity) physics that allows for decoupling and multiple equilibria in this model. We do this using mechanism-denial experiments,

turning off various physics (either by setting parameters to zero or by setting diagnostic parameters that in principle depend on other model variables to a constant) and examining the results. An explicit description of each experiment is provided throughout the analysis below. Throughout, we emphasize new lessons learned thanks to the use of the simple model. We discuss in the conclusions the value and expected applicability of these new lessons given the simplicity of the model.

a. Hysteresis in CO_2

Figure 3 shows several equilibrium state variables in the CO_2 hysteresis. We solve the system for CO_2 values ranging from 280 to 2500 ppm. Coupled solutions (plotted in red) are characterized by lower surface temperatures (Fig. 3a) due to the albedo effect of the cloud layer, as in Schneider et al. (2019). Additionally, cloud-top longwave cooling is higher in the coupled case (Fig. 3b), driving convection and providing the cloud layer with a moisture source from the surface (Lilly 1968; Bretherton and Wyant 1997).

Following the coupled solutions in Fig. 3, as CO_2 increases, the emissivity of the troposphere ϵ_i increases, both directly from its dependence on CO_2 as well as from the water vapor feedback [Eq. (17)]. As in Schneider et al. (2019), this causes a decrease in net longwave cooling across the mixed layer ΔF_R (Fig. 3b) until at around 1750 ppm the longwave cooling is no longer strong enough to drive convection, and the model predicts only decoupled solutions at higher CO_2.

The entrainment closure [Eq. (10)] predicts that, all other things being equal, entrainment should weaken with longwave cooling. However, in Fig. 3i, we see a slight strengthening of entrainment with CO_2. This is because a warmer mixed layer leads to a weaker inversion strength $\Delta \theta_v^{i-c}$, which allows for stronger mixing across the cloud top (McMichael et al. 2019; Zapata et al. 2020).

Figure 3d plots the decoupling criterion in red and the coupling criterion in blue. At low CO_2, the coupled solution predicts positive buoyancy fluxes beneath the cloud from Eq. (28), but as CO_2 increases, the buoyancy fluxes beneath the cloud approach zero. Since we have enacted a strict decoupling criterion, negative buoyancy fluxes beneath the cloud lead to decoupling, so for CO_2 values higher than the CO_2 where the buoyancy flux is zero, only decoupled solutions exist.

In the decoupled state, without the main moisture source from the surface, the small source of moisture from mixing with the SML, w_e^{SML}, is insufficient to sustain a cloud against entrainment drying from the troposphere, w_e^{inv}. For the parameter regime explored in this work, this results in a LWP of zero in the DML, and the cloud-base height is equal to the cloud-top height (i.e., a zero-thickness cloud layer; Figs. 3g,h). Additionally, the LWP in the SML is zero for all decoupled regimes explored by this model. This causes a low albedo α and cloud emissivity ϵ_c, leading to higher surface temperatures and weaker longwave cooling (Fig. 3e). Following the decoupled solutions, decreasing CO_2 does not lead to recoupling at 1750 ppm, where decoupling occurred due to increasing CO_2 when following the coupled solutions. Instead, CO_2 must be decreased down to 500 ppm in order for the stratification between the SML and DML to become unstable and allow for convection between the surface and DML [Fig. 3d; Eq. (33)]. In other words, for a given value of CO_2 between 500 and 1750 ppm, there are multiple equilibria in which the layer could be either coupled or decoupled depending on its initial condition.

In general, our mixed-layer model yields similar results to those of Schneider et al. (2019), who used an LES. In both this model and the LES, increasing CO_2 causes (i) an increase in latent heat release from the surface due to enhanced seawater evaporation, (ii) a decrease in longwave cooling due to an opaquer troposphere and a lower cloud emissivity, (iii) a decrease in LWP, (iv) a decoupling of the cloud layer at high CO_2, and (v) an abrupt increase in SST following decoupling.

Though our results are qualitatively similar to the LES study performed by Schneider et al. (2019), the exact range of CO_2 values that show bistability is slightly different between this model (500–1750 ppm) and the LES study (where the range is not possible to determine exactly due to the finite resolution in CO_2 but is roughly from $\sim$300 to $\sim$1200 ppm).

Though various model parameters (indicated with a star in Table 1) were tuned to give the best agreement with Schneider et al. (2019) and other constants were taken directly from their work, differences in model complexity make it impossible to perfectly replicate their results, especially considering the sensitivity of the LES to small changes in model parameters [e.g., sensitivity to large-scale divergence in Schneider et al. (2019)]. We emphasize that the goal of this work is to qualitatively explore the fundamental mechanisms in the stratocumulus instability, as we demonstrate below.

In their hysteresis in CO_2, Schneider et al. (2019) cited the importance of amplifying cloud cover–SST feedbacks as well as the water vapor feedback for the abrupt stratocumulus cloud breakup. To test this assertion as well as to explore the importance of other processes such as entrainment, we perform a suite of mechanism-denial experiments in Fig. 4.

In the experiments shown in the first row of Fig. 4, we create a noninteractive SST by making T_s a function of CO_2 only to remove cloud cover–SST feedbacks:

$$T_s = T_{so} + 3 \log_2\left(\frac{CO_2}{280}\right),$$

where T_{so} is the surface temperature in the baseline coupled solution at 280 ppm. The solution is very similar to the baseline solution in Fig. 3, plotted as faint lines in Fig. 4 for easy comparison. The weakening of longwave cooling and strengthening of cloud-top entrainment are still seen with increasing CO_2, and decoupling occurs at high CO_2 with multiple equilibria. This indicates that amplifying cloud cover–SST feedbacks is not essential for decoupling in this model, though it does affect the range of CO_2 values that exhibit multiple equilibria.

In the experiments shown in the second row of Fig. 4, we restore the interactive SST but remove the contribution of water vapor to the inversion emissivity by setting $B = 0$ in Eq. (17). The most notable difference between the no water vapor feedback case and the baseline case is that it takes over twice as much CO_2 for decoupling to occur. As in Schneider et al. (2019), at 1000 ppm, the reduction in longwave cooling is only half as much in the no water vapor feedback case than in the baseline case. However, abrupt decoupling does still occur, just at a higher CO_2 than the baseline case. Therefore, in this model the water vapor feedback affects the onset of decoupling but is not necessary for decoupling to occur.

In the experiment shown in the third row of Fig. 4, we perform the above two tests simultaneously, turning off both the interactive SST and the water vapor feedback. We conclude that even with both cloud cover–SST feedbacks and the water vapor feedback disabled, abrupt stratocumulus breakup still occurs in this model. Interestingly, Schneider et al. (2019) cited cloud cover–SST feedbacks and the water vapor feedback as crucial components of the abrupt stratocumulus cloud breakup in their model, but in our model decoupling occurs without either of these feedbacks. This suggests that these feedbacks may not be critical for the abrupt breakup of stratocumulus clouds with increasing CO_2. However, we recognize that the simplicity of our mixed-layer model may mean that
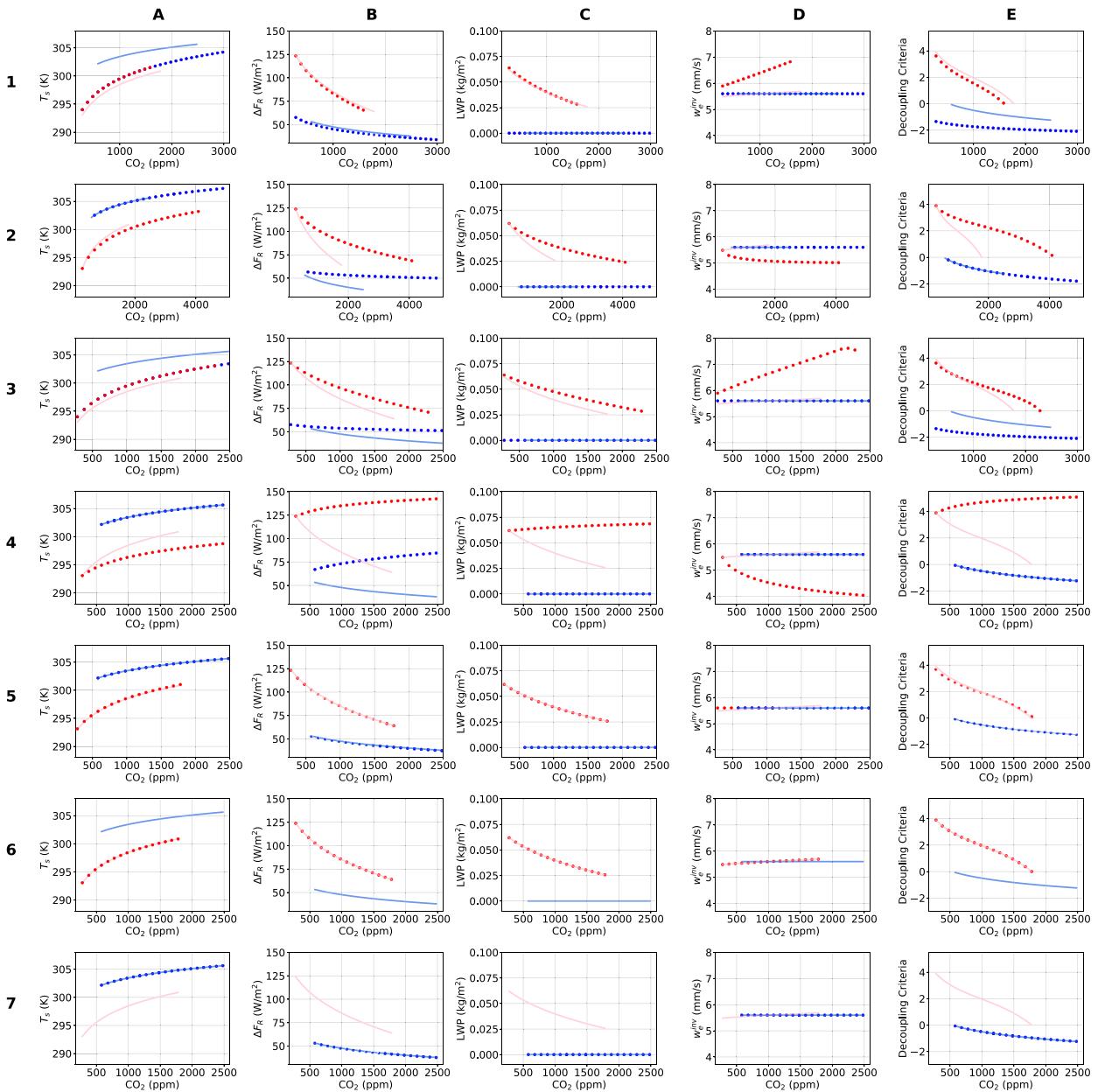
FIG. 4. Summary of mechanism-denial experiments for hysteresis in CO_2. (first row) Noninteractive SST, only a function of CO_2. (second row) No water vapor feedback, where inversion emissivity is only a function of CO_2 [$B = 0$ in Eq. (17)]. (third row) Both the first and second rows. (fourth row) Constant inversion emissivity ϵ_i. (fifth row) Constant cloud-top entrainment w_e^{inv}. (sixth row) Constant cloud emissivity $\epsilon_c = 1$. (seventh row) Constant cloud emissivity $\epsilon_c = 0.45$. (a) SST. (b) Net longwave cooling. (c) Cloud LWP. (d) Cloud-top entrainment rate. (e) Decoupling criteria for each experiment. Transparent lines show the baseline simulation from Fig. 3.

these processes may still be important in the parameter regime relevant to the presently observed climate. Further studies of the importance of these feedbacks should be done with more realistic models.

In Schneider et al. (2019), decoupling at higher CO_2 was attributed to the reduction in longwave cooling caused by the increased emissivity of the troposphere. To test this assertion, in the fourth row of Fig. 4, we set the inversion emissivity to a constant [$A = B = 0$ in Eq. (17)]. In Fig. 4b (the fourth row), we see no reduction in longwave cooling, which translates to no decrease in the decoupling criterion in Fig. 4e. We ran the model out to 10 000 ppm, and still, we found no critical CO_2 where the model decouples and the stratocumulus clouds dissipate. This is consistent with the results from Schneider et al. (2019) that stratocumulus breakup is caused by the increase in emissivity of the free troposphere with CO_2.
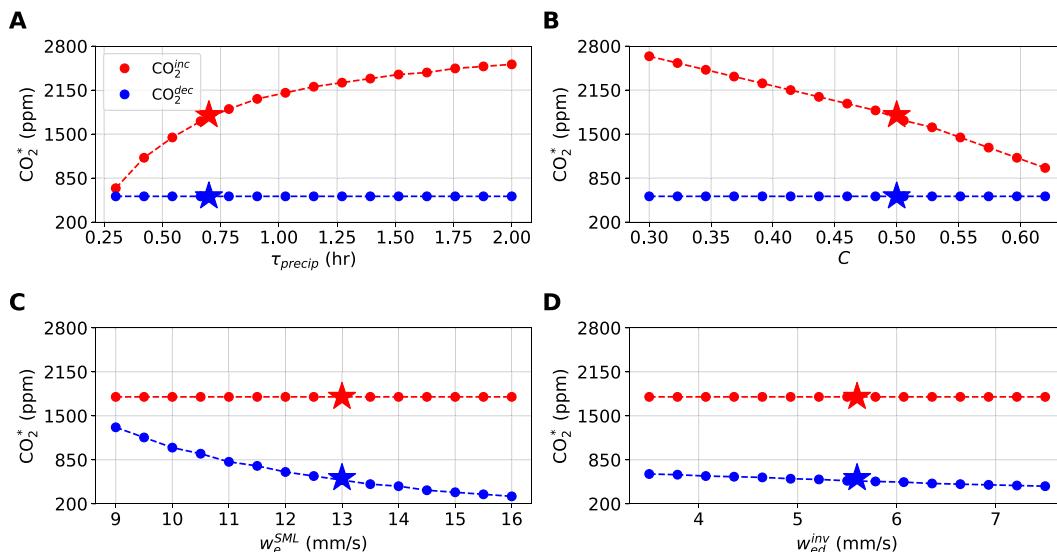
FIG. 5. Critical CO_2 where transition occurs when increasing CO_2 (CO_2^{inc}) and decreasing CO_2 (CO_2^{dec}) as a function of (a) precipitation time scale τ_{precip}, (b) cloud-top entrainment efficiency C, (c) entrainment between SML and DML w_e^{SML}, and (d) entrainment between DML and troposphere w_{ed}^{inv}. The difference between the red and blue lines represents the width of the hysteresis. Stars indicate the bounds of the hysteresis for the baseline solution from Fig. 3.

In the baseline solution, along with a weakening of longwave cooling with increasing CO_2, there is also a slight strengthening of the cloud-top entrainment, which could also lead to decoupling (Bretherton and Wyant 1997). In the fifth row of Fig. 4, we set the cloud-top entrainment to the background constant value specified in Table 1 w_{ed}^{inv} for both the coupled and decoupled case and find very little difference between this test and the baseline solution, indicating that enhanced entrainment is not a necessary mechanism for hysteresis in CO_2 to exist in our model.

In all of the above-outlined sensitivity tests, the existence of multiple equilibria remains robust. In their hysteresis in SST, Bellon and Geoffroy (2016) attributed the existence of multiple equilibria to the cloud radiative effect. On the one hand, clouds with high LWP [see Fig. 4c] would have large longwave emissivity, leading to strong longwave cooling, which maintains the cloud layer. Clouds with a low LWP, on the other hand, would have a small emissivity and weak longwave cooling, again maintaining the low LWP. To test this, we set the cloud emissivity in our two final mechanism-denial experiments to a constant, independent of LWP. In the sixth row of Fig. 4, $\epsilon_c = 1$, and in the seventh row of Fig. 4, $\epsilon_c = \epsilon_{co}$. For the high (low) emissivity case, only coupled (decoupled) solutions exist because the longwave cooling is never weak (strong) enough to support a decoupled (coupled) solution. Therefore, in our model the dependence of cloud emissivity on liquid water path is necessary for multiple equilibria to exist, consistent with Bellon and Geoffroy (2016).

In the above experiments, we see that even processes that are not considered essential for decoupling to occur can still affect the onset of decoupling. In Schneider et al. (2019), the critical CO_2 where decoupling occurs as well as the width of the hysteresis was found to be very sensitive to model parameters

such as large-scale subsidence, but the computational cost of the model precluded further sensitivity tests.

In Fig. 5, we explore how the width of the hysteresis (i.e., the range of SST or CO_2 values for which multiple equilibria exist) varies with uncertain model parameters. In each panel, we study the sensitivity of the width of the hysteresis to individual model parameters. When following the coupled solutions, the CO_2 value where decoupling occurs when increasing CO_2 (CO_2^{inc}) is plotted in red, while the CO_2 value where recoupling occurs when following the decoupled solutions and decreasing CO_2 (CO_2^{dec}) is plotted in blue. The difference between these two curves gives the width of the hysteresis. Of specific interest are the precipitation time scale τ_{precip} and the entrainment efficiency C, both of which are ill constrained because of the complexity of cloud microphysics and aerosol–cloud interactions (Gerber 1996; Jiang et al. 2002; Bretherton et al. 2007; Wang and Feingold 2009; Ackerman et al. 2009; Uchida et al. 2010).

Unsurprisingly, we find that the CO_2 value where decoupling occurs, CO_2^{inc}, is very sensitive to both of these parameters. In Fig. 5a, decreasing τ_{precip} (increasing the precipitation rate) leads to decoupling at a lower CO_2. An order of magnitude change in the precipitation time scale leads to nearly a 2000-ppm increase in CO_2^{inc}, meaning that the response of CO_2^{inc} to a tenfold increase in the precipitation time scale is larger than the width of the hysteresis (the difference between the red and blue curves in Fig. 5) in the baseline case. A decreased precipitation time scale leads to enhanced evaporative cooling beneath the cloud base, which stabilizes the layer and inhibits convection (Stevens et al. 1998). Precipitation has no effect on the CO_2 where recoupling occurs CO_2^{dec} because, in our model, LWP and therefore precipitation is zero in a decoupled case. The time scale of precipitation in reality

depends on the density of cloud condensation nuclei (CCN), on the rate of gravitational settling wherein larger droplets collect smaller droplets as they fall through the cloud layer, and on turbulence effects that can accelerate the merging of droplets (Falkovich et al. 2002), all of which affect the average size of the water droplet (Ackerman et al. 2009). Future work could investigate how these processes affect the width of the hysteresis in a more realistic model.

The cloud-top entrainment efficiency C is another uncertain parameter known to play an important role in simulations of stratocumulus cloud dynamics using mixed-layer models; therefore, in Fig. 5b, we test how C affects the width of the CO_2 hysteresis. The model demonstrates strong sensitivity to the entrainment efficiency, showing nearly a 2000-ppm decrease of CO_2^{inc} for a doubling of C. Once again, CO_2^{dec} shows no sensitivity, since in decoupled solutions we set a constant background entrainment rate w_{ed}^{inv}. For models run under prescribed SST, cloud-top entrainment plays a key role in decoupling with increasing SST by stabilizing the air column through entrainment warming (Bretherton and Wyant 1997), and our results here indicate that entrainment will play an important role in the timing of decoupling with increasing CO_2 as well. Understanding how entrainment is affected by, for example, cloud microphysics is an active area of research (Bretherton et al. 2007; Uchida et al. 2010; Wood 2012). When sedimentation feedbacks are included, high CCN concentrations lead to smaller droplets that keep liquid water closer to the entrainment zone and therefore to more efficient entrainment that decreases cloud LWP. This can cancel up to 50% of the increase in albedo due to the Twomey effect (Uchida et al. 2010). Additionally, entrainment–evaporation feedbacks wherein small droplets evaporate more readily, increasing turbulent mixing, also affect the entrainment rate at the cloud top (Hoffmann et al. 2020).

While our model does not include cloud microphysics, we can learn about its effects on the hysteresis and multiple equilibria indirectly from our model results, using knowledge of how CCN concentration affects precipitation and entrainment. In a parameter regime with abundant CCNs, decreasing CCN concentration should lead to an increase in precipitation efficiency (corresponding to lower values of τ_{precip} in Fig. 5a) by increasing the average size of cloud droplets (Twomey 1977; Ackerman et al. 2009). In our model, this corresponds to a lower CO_2^{inc}, as seen in Fig. 5a. Additionally, decreasing CCN concentration could lead to a decrease in entrainment efficiency (corresponding to lower values of C in Fig. 5b) by creating larger cloud droplets that sediment out of the entrainment zone rather than evaporating and causing evaporative cooling and lead to less efficient entrainment (Bretherton et al. 2007; Uchida et al. 2010). Based on the results of our model, this could lead to an increase in CO_2^{inc}. The question of which process would dominate for varying CCN concentration is outside the scope of this study but would be interesting to examine using models that include cloud microphysical effects.

Our treatment of the decoupled case with two stacked mixed layers (surface and decoupled mixed layers, denoted SML and DML, correspondingly), following Turton and Nicholls (1987),

is highly idealized, especially with our added simplifications that the entrainment rate between the SML and DML as well as the cloud-top entrainment rate are constant. In Figs. 5c and 5d, we explore how sensitive the lower CO_2 boundary of the multiple equilibria region CO_2^{dec} is to the chosen value of each of the two entrainment rates. Our model shows high sensitivity of CO_2^{dec} to the entrainment rate between the SML and DML, w_e^{SML}, and comparatively little sensitivity to the cloud-top entrainment, w_{ed}^{inv}. For decreasing CO_2, the critical value at which recoupling occurs CO_2^{dec} happens when the stratification between the SML and DML is no longer stable ($\theta_{DML} = \theta_{SML}$ at z_{SML}). This can be written as

$$T_{DML}\left(\frac{P_{SML}}{P_o}\right)^{R/c_p}(1 + \delta q_{DML}) = T_{SML}\left(\frac{P_{SML}}{P_o}\right)^{R/c_p}(1 + \delta q_{SML}),$$

(35)

where T_{DML} is the temperature in the DML at z_{SML}^+ (just above the altitude separating the SML and DML), and T_{SML} is the temperature in the SML at z_{SML}^- (just below the altitude separating the SML and DML), calculated from MSE and q_t in each layer. Increasing w_e^{SML} moistens the DML, such that CO_2 must be decreased to very low levels in order for longwave cooling to become strong enough to decrease T_{DML} and have $\theta_{DML} \leq \theta_{SML}$. In a decoupled state, the DML is very dry, and therefore cloud-top entrainment does not lead to as much evaporative cooling and has a much smaller effect on the dynamics of the DML compared to mixing with the SML. This leads to a much smaller sensitivity to w_{ed}^{inv} (cf. Figs. 5c,d). Again, CO_2^{inc} does not depend on either entrainment rate since that parameterization is only included in the decoupled state. Future iterations of this model could include dynamic entrainment rates and boundary layer thicknesses in the decoupled case. Additionally, this model could be used to explore regimes with cloudy decoupled layers.

b. Hysteresis in SST

Previous work by Bellon and Geoffroy (2016) used an LES to demonstrate how the cloud radiative effect allowed for multiple equilibria with proscribed constant SST. As a test for our model, we replaced the surface energy balance with

$$T_s = T_s^{fixed},$$

(36)

with T_s^{fixed} representing the prescribed SST with which the model is forced. CO_2 is given a constant value of 280 ppm throughout this series of model experiments. In previous sections, we demonstrated that increased inversion emissivity was vital for decoupling to occur. In the model configuration used above, the inversion temperature was a function of CO_2 to represent warming in the tropics due to CO_2 changes. Therefore, for the fixed SST case, we rewrite the parameterization of inversion temperature as $T_i = T_s - \Gamma_i (z_i - z_{io})$, an approximation consistent with the current observed relation between the inversion and surface temperatures (Nicholls 1984). Once again assuming constant relative humidity, ϵ_i now increases with SST through the water vapor feedback alone.
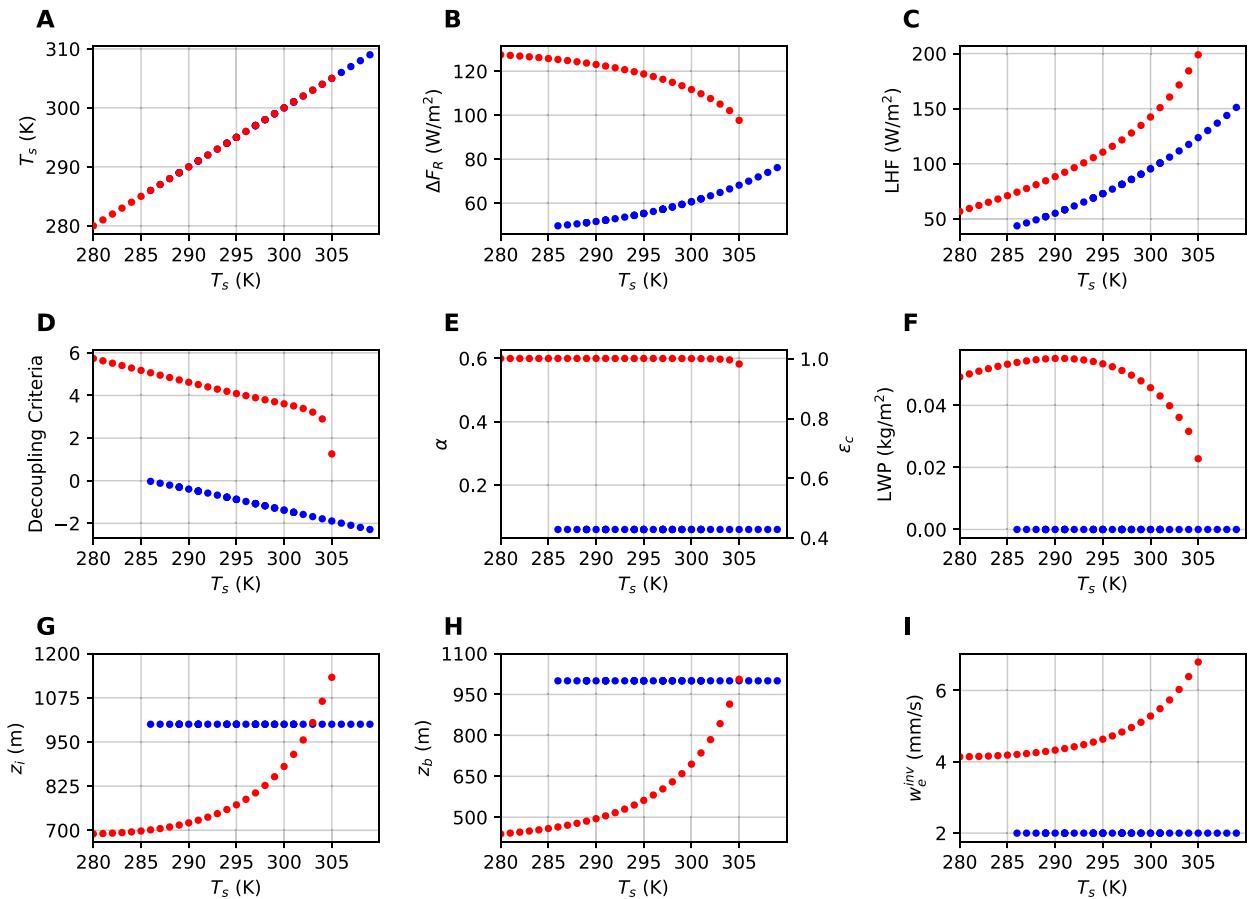
FIG. 6. Hysteresis in SST. Red dots indicate coupled solutions while blue dots indicate decoupled solutions. (a) SST (T_s). (b) Net long-wave cooling across mixed layer. (c) Latent heat flux from surface. (d) Decoupling/coupling criteria [Eq. (28) for coupled solutions and the negative of Eq. (33) for decoupled solutions]. Note that the coupled solutions have been scaled up for plotting purposes. (e) Albedo and cloud emissivity. (f) Cloud liquid water path. (g) Mixed-layer depth. (h) Cloud base. (i) Cloud-top entrainment rate.

Figure 6 shows the results of our model in the fixed SST case. Though the SST is the same for both a coupled and de-coupled case, there are multiple equilibria between surface temperatures of 286 and 305 K. In the LES study of Bellon and Geoffroy (2016), the SST range considered did not reveal the entire hysteresis because the low SST at which coupling occurs was not reached. Their SST range extended down to 288 K, and in our model coupling occurs at 286 K, suggesting that simply expanding their SST range may have revealed the left side of the hysteresis. In addition, the critical SST where decoupling occurred was around 294 K, while ours is at 305 K. To understand this 10-K difference, first we examine the mechanisms behind decoupling in our mixed-layer model under prescribed increasing SST.

Starting from an SST of 280 K in a coupled state, increasing SST both weakens longwave cooling (Fig. 6b) due to the water vapor feedback and strengthens cloud-top entrainment (Fig. 6i), both of which lead to a decreasing decoupling criterion (Fig. 6d). As in the LES study of Bellon and Geoffroy (2016), LWP has a maximum at about 292 K and then rapidly decreases due to the enhanced entrainment. The combination of enhanced entrainment and weakened longwave cooling

decreases the buoyancy fluxes at the cloud base [decoupling criterion; Eq. (28)], but at 305 K, decoupling happens very abruptly. This is because of the decrease in cloud emissivity (Fig. 6e) when cloud LWP dips past a threshold value set by the liquid water longwave absorption coefficient κ appearing in Eq. (16). This decrease in cloud emissivity results in a large decrease in net longwave cooling and results in negative buoyancy fluxes beneath the cloud base and therefore in decoupling. This effect was also noted by Bellon and Geoffroy (2016), who saw decoupling at 294 K (an 11-K cooler decoupling threshold than in our model). This difference from Bellon and Geoffroy (2016) in the critical SST at which decoupling occurs could be partially explained by the fact that their κ was nearly half of ours (which is taken from the parameterization of radiative cloud effects in the community atmospheric model; Neale et al. 2010), leading to a reduction in cloud emissivity at a higher LWP. Other possible explanations for the difference in the critical SST likely exist in our parameterizations of entrainment and precipitation as well as the major difference in model complexity. It would have been simple to make the critical SST more similar, for example, by increasing the entrainment efficiency C from 0.5 to 0.67 in our
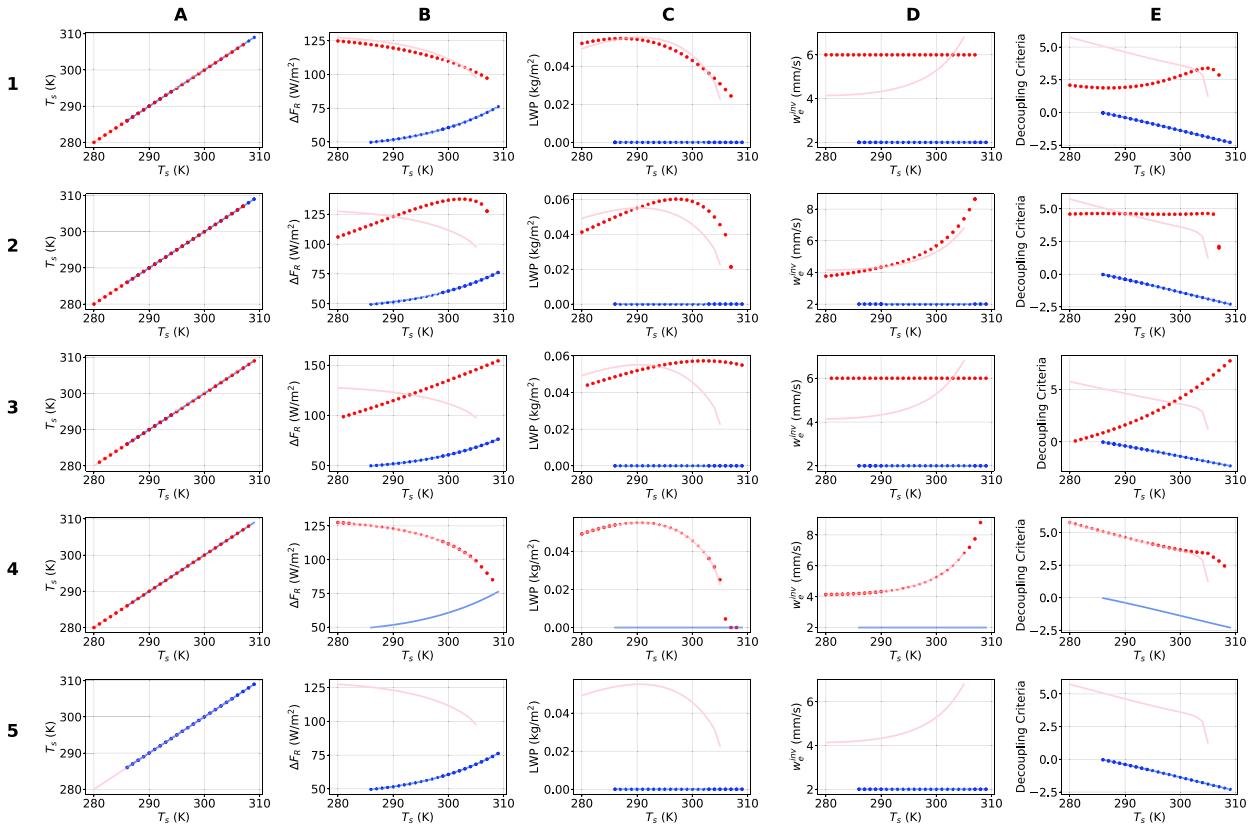
FIG. 7. Summary of mechanism-denial experiments for hysteresis in SST. (first row) Constant cloud-top entrainment w_e^{inv}. (second row) Constant inversion emissivity, ϵ_i. (third row) Both the first and second rows. (fourth row) Constant cloud emissivity $\epsilon_c = 1$. (fifth row) Constant cloud emissivity, $\epsilon_c = 0.45$. (a) SST. (b) Net longwave cooling. (c) Cloud LWP. (d) Cloud-top entrainment rate. (e) Decoupling criteria for each experiment. Transparent lines show the baseline simulation from Fig. 6.

model, which allows decoupling to occur at 295 K, which is much more consistent with Bellon and Geoffroy (2016). In the interest of changing the minimum number of parameters in the translation from the CO_2 to the SST hysteresis, we did not retune the model for the SST hysteresis. Model parameters marked with a star in Table 1 indicate parameters tuned to best match the CO_2 hysteresis in Schneider et al. (2019).

Additionally, Bellon and Geoffroy (2016) prescribed the radiative effect of clouds as a function of liquid water path alone, assuming constant fluxes from the surface and free troposphere. This neglects the effect of the water vapor feedback on the emissivity of the free troposphere, which may also contribute to differences in our results.

As in the analysis of the CO_2 hysteresis, we perform a series of mechanism-denial experiments, shown in Fig. 7. As enhanced entrainment and weakening longwave cooling can both decouple the mixed layer, we begin by shutting off each of these mechanisms in turn. In the first row of Fig. 7, we set the entrainment to a constant and find that the weakening of longwave cooling due to the water vapor feedback does not prevent decoupling and only shifts the decoupling SST from 305 to 307 K. Alternatively, in the second row of Fig. 7, setting the emissivity of the troposphere to a constant does not inhibit decoupling either, as enhanced entrainment eventually

decreases the LWP such that longwave cooling dramatically decreases. It is only when both of these mechanisms are shut off that the mixed layer stays coupled, even up to 320 K (third row of Fig. 7). This indicates that in the fixed SST hysteresis both enhanced entrainment and weakening longwave cooling can cause decoupling on their own.

In either case, decoupling happens very abruptly due to the decrease of LWP caused by both mechanisms (cloud-top entrainment and troposphere emissivity). Even when entrainment is constant, the weakening of longwave cooling in the first row of Fig. 7 leads to a warmer mixed layer, which increases the saturation point and therefore decreases the liquid water ratio in the mixed layer. Enhanced entrainment decreases LWP both by enhanced drying but also by warming the mixed layer and allowing more water to exist in vapor form. Abrupt decoupling occurs when the LWP passes a threshold at which the emissivity of the cloud layer is no longer near unity and longwave cooling begins to weaken.

Finally, we test the assertion by Bellon and Geoffroy (2016) that multiple equilibria are caused by the cloud radiative effect by setting the emissivity of the cloud to unity (experiment shown on fourth row of Fig. 7) and to the minimum value of $\epsilon_{co} = 0.45$ (fifth row of Fig. 7), regardless of LWP. As in the CO_2 hysteresis, only coupled (decoupled) solutions exist when
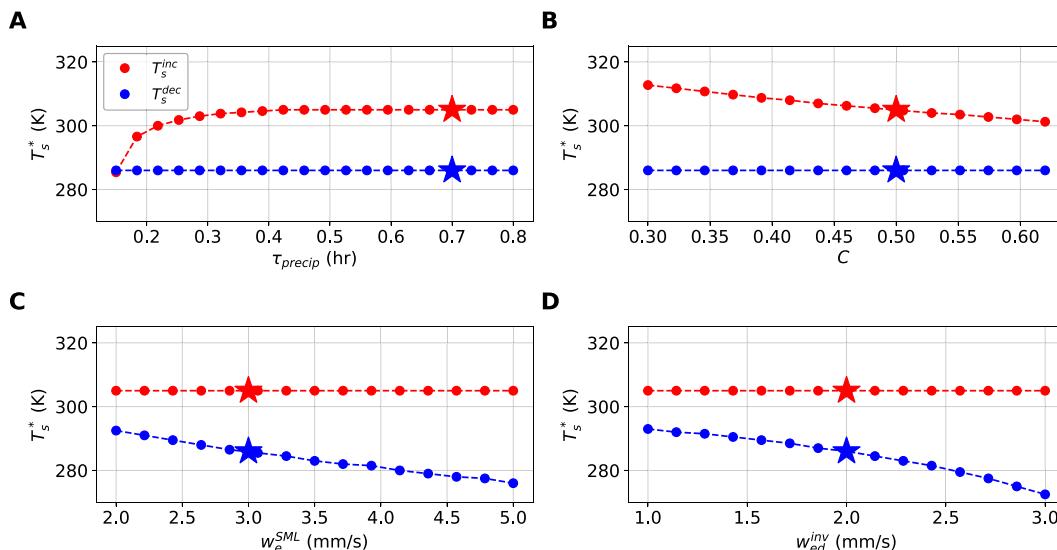
FIG. 8. Critical T_s where transition occurs when increasing T_s T_s^{inc} and decreasing T_s T_s^{dec} as a function of (a) precipitation time scale τ_{precip}, (b) cloud-top entrainment efficiency C, (c) entrainment between SML and DML w_e^{SML}, and (d) entrainment between DML and troposphere $w_{\text{ed}}^{\text{inv}}$. The difference between the red and blue lines represents the width of the hysteresis.

$\epsilon_c = 1$ (ϵ_{co}). Once again, our model requires the dependence of cloud emissivity on LWP to show multiple equilibria, consistent with Bellon and Geoffroy (2016).

We also use the computational efficiency of the model to study the sensitivity of the SST hysteresis to various model parameters in Fig. 8. In Fig. 8a, decoupling occurs at lower SST values when the precipitation time scale is very small (precipitation rate is very fast) because of the enhanced evaporative cooling beneath the cloud base. At higher τ_{precip}, the SST at which decoupling occurs T_s^{inc} asymptotes to around 305 K because at these time scales all of the precipitation evaporates before it reaches the surface, and the net precipitation flux out of the mixed layer vanishes: $\Delta F_P = 0$. In Fig. 8b, we vary the entrainment efficiency C and find similarly to the CO_2 hysteresis case that increasing C leads to decoupling at lower T_s due to enhanced entrainment warming at the cloud top. In both Figs. 8a and 8b, T_s^{dec} shows no sensitivity to either parameter since there is no LWP and a constant cloud-top entrainment in the decoupled state.

In Fig. 8c, we test the sensitivity of T_s^{dec} to entrainment mixing between the SML and the DML. Increasing w_e^{SML} decreases T_s^{dec} by moistening the DML and requiring very low surface temperatures to decrease θ_v^{DML} beyond the threshold in Eq. (33), similar to the CO_2 hysteresis. In Fig. 8d, we test the sensitivity of the model to $w_{\text{ed}}^{\text{inv}}$. Unlike in the CO_2 hysteresis, there is a strong sensitivity to the cloud-top entrainment rate due to its larger size relative to w_e^{SML}. The hysteresis in CO_2 and SST demonstrates similar sensitivities to these four model parameters. Though the prescribed SST case ignores cloud cover–SST feedbacks, it does provide an interesting framework for a case study of advected columns over warm ocean water. In both cases, precipitation and cloud-top entrainment play a large role in determining the onset of decoupling in

SST, and the effects of cloud microphysics on the bistability of stratocumulus-topped boundary layers could be studied with higher complexity models that include an explicit microphysical parameterization.

4. Conclusions

In this work, we investigated hysteresis and multiple equilibria of stratocumulus clouds that were previously studied using LES (Bellon and Geoffroy 2016; Schneider et al. 2019) with implications for cloud feedbacks in warm climates. Though LES have been used to investigate the role of physical processes in the maintenance of stratocumulus-topped boundary layers (e.g., Matheou and Teixeira 2019), a study of the sensitivity of the hysteresis behavior has not yet been done. For this purpose, we developed a mixed-layer model adapted to include a surface energy balance and the ability to model decoupled solutions using "stacked" mixed layers following Turton and Nicholls (1987). Using this model, we were able to reproduce the hysteresis as a function of SST (Bellon and Geoffroy 2016) and CO_2 (Schneider et al. 2019). The simplicity of the model allowed us to perform mechanism-denial experiments by easily switching off various physics. The computational efficiency of the model allowed us to perform a suite of sensitivity tests to find which parameters control the hysteresis behavior.

Schneider et al. (2019) deduced from their experiments that a dynamic SST, cloud–SST feedbacks, and the water vapor feedback were crucial for the abrupt stratocumulus cloud breakup to occur for higher CO_2 values. Interestingly, we find that neither cloud cover–SST feedbacks nor the water vapor feedback are required for decoupling to occur in our model. Instead, only an increase in troposphere emissivity with CO_2 is required. We found in extensive sensitivity experiments that the main nonlinearity needed to support the existence of

multiple equilibria either as a function of fixed SST or of CO_2 is provided by the dependence of cloud emissivity on liquid water path, as suggested by Bellon and Geoffroy (2016) for their SST-driven hysteresis. When this nonlinearity is turned off the multiple equilibria cease to exist regardless of the many other nonlinearities that are still present. The width of the hysteresis (i.e., the range of CO_2 or SST in which multiple equilibria exist) in our model also demonstrates strong sensitivity to processes that depend in reality on cloud microphysics (precipitation and entrainment parameterizations in our model). In their study of the hysteresis in fixed SST, Bellon and Geoffroy (2016) attributed the decoupling and stratocumulus dissipation at higher SST to the strong enhancement of entrainment with increasing SST but did not examine the role of the water vapor feedback. We find that decoupling with increasing SST can occur either via the enhanced entrainment or via increased inversion emissivity due to the water vapor feedback in our model.

The model used here is highly idealized and is not meant for quantitative predictions such as the precise SST or CO_2 at which stratocumulus coupling or decoupling occurs. Instead, it is designed as a tool to identify zeroth-order physical mechanisms and dependencies using mechanism-denial experiments and to perform extensive sensitivity studies with respect to key model parameters. As such, there are many simplifying assumptions made in this model. For example, to model the decoupled state in the simplest configuration, we adopted a "stacked" mixed-layer model with prescribed constant thickness of each layer as well as constant entrainment rates at each interface. This allowed us to explore the minimum physics responsible for the existence and character of the hysteresis at the cost of quantitative accuracy. It is important to understand the applicability of the above-summarized lessons learned using the mechanism-denial experiments based on an idealized model such as the one used here. Finding that a certain process is or is not essential for a certain equilibrium state to be present (e.g., that the water vapor feedback can cause decoupling at higher SST or that dynamic SST is not required for the existence of multiple equilibria as a function of CO_2) adds to the fundamental qualitative understanding of the processes involved. A feedback that is found not to be essential for decoupling to occur, for example, may still contribute quantitatively by affecting the critical SST or CO_2 at which decoupling occurs, as shown above. The findings of the idealized model motivate further experiments with more realistic models that can then address these issues more quantitatively.

The stratocumulus instability with CO_2 may be relevant to past equable climates (e.g., Eocene; Schneider et al. 2019). This joins other cloud feedbacks that have been advanced as explanations for such equable climates, including polar stratospheric clouds (Sloan and Pollard 1998; Kirk-Davidoff et al. 2002), convective wintertime Arctic clouds (Abbot and Tziperman 2008a), or low clouds suppressing polar air formation (Cronin and Tziperman 2015). A study of how these mechanisms interact could benefit from simple cloud models like the one employed here.

REFERENCES

Abbot, D. S., and E. Tziperman, 2008a: A high latitude convective cloud feedback and equable climates. *Quart. J. Roy. Meteor. Soc.*, **134**, 165–185, https://doi.org/10.1002/qj.211.

——, and ——, 2008b: Sea ice, high latitude convection, and equable climates. *Geophys. Res. Lett.*, **35**, L03702, https://doi.org/10.1029/2007GL032286.

——, and ——, 2009: Controls on the activation and strength of a high-latitude convective cloud feedback. *J. Atmos. Sci.*, **66**, 519–529, https://doi.org/10.1175/2008JAS2840.1.

Ackerman, A. S., and Coauthors, 2009: Large-eddy simulations of a drizzling, stratocumulus-topped marine boundary layer. *Mon. Wea. Rev.*, **137**, 1083–1110, https://doi.org/10.1175/2008MWR2582.1.

Bellon, G., and O. Geoffroy, 2016: Stratocumulus radiative effect, multiple equilibria of the well-mixed boundary layer and transition to shallow convection. *Quart. J. Roy. Meteor. Soc.*, **142**, 1685–1696, https://doi.org/10.1002/qj.2762.

Bretherton, C. S., 1997: Convection in stratocumulus-topped atmospheric boundary layers. *The Physics and Parameterization of Moist Atmospheric Convection*, Roger K. Smith, Ed., Springer, 127–142.

——, and M. C. Wyant, 1997: Moisture transport, lower-tropospheric stability, and decoupling of cloud-topped boundary layers. *J. Atmos. Sci.*, **54**, 148–167, https://doi.org/10.1175/1520-0469(1997)054<0148:MTLTSA>2.0.CO;2.

——, P. N. Blossey, and J. Uchida, 2007: Cloud droplet sedimentation, entrainment efficiency, and subtropical stratocumulus albedo. *Geophys. Res. Lett.*, **34**, L03813, https://doi.org/10.1029/2006GL027648.

Cronin, T. W., and E. Tziperman, 2015: Low clouds suppress Arctic air formation and amplify high-latitude continental winter warming. *Proc. Natl. Acad. Sci. USA*, **112**, 11 490–11 495, https://doi.org/10.1073/pnas.1510937112.

Falkovich, G., A. Fouxon, and M. G. Stepanov, 2002: Acceleration of rain initiation by cloud turbulence. *Nature*, **419**, 151–154, https://doi.org/10.1038/nature00983.

Gerber, H., 1996: Microphysics of marine stratocumulus clouds with two drizzle modes. *J. Atmos. Sci.*, **53**, 1649–1662, https://doi.org/10.1175/1520-0469(1996)053<1649:MOMSCW>2.0.CO;2.

Gettelman, A., 2015: Putting the clouds back in aerosol–cloud interactions. *Atmos. Chem. Phys.*, **15**, 12 397–12 411, https://doi.org/10.5194/acp-15-12397-2015.

Hahn, C. J., and S. G. Warren, 2007: A gridded climatology of clouds over land (1971-96) and ocean (1954-97) from surface observations worldwide. Oak Ridge National Laboratory, Carbon Dioxide Information Analysis Center, accessed 20 May 2022, https://doi.org/10.3334/CDIAC/cli.ndp026e.

Hoffmann, F., F. Glassmeier, T. Yamaguchi, and G. Feingold, 2020: Liquid water path steady states in stratocumulus: Insights from process-level emulation and mixed-layer theory. *J. Atmos. Sci.*, **77**, 2203–2215, https://doi.org/10.1175/JAS-D-19-0241.1.

Jiang, H., G. Feingold, and W. R. Cotton, 2002: Simulations of aerosol-cloud-dynamical feedbacks resulting from entrainment of aerosol into the marine boundary layer during the Atlantic Stratocumulus Transition Experiment. *J. Geophys. Res.*, **107**, 4813, https://doi.org/10.1029/2001JD001502.

Kirk-Davidoff, D. B., D. P. Schrag, and J. G. Anderson, 2002: On the feedback of stratospheric clouds on polar climate. *Geophys. Res. Lett.*, **29**, 1556, https://doi.org/10.1029/2002GL014659.

Klein, S. A., and D. L. Hartmann, 1993: The seasonal cycle of low stratiform clouds. *J. Climate*, **6**, 1587–1606, https://doi.org/10.1175/1520-0442(1993)006<1587:TSCOLS>2.0.CO;2.

Lilly, D. K., 1968: Models of cloud-topped mixed layers under a strong inversion. *Quart. J. Roy. Meteor. Soc.*, **94**, 292–309, https://doi.org/10.1002/qj.49709440106.

Loeb, N. G., and Coauthors, 2018: Clouds and the Earth's Radiant Energy System (CERES) Energy Balanced and Filled (EBAF) top-of-atmosphere (TOA) edition-4.0 data product. *J. Climate*, **31**, 895–918, https://doi.org/10.1175/JCLI-D-17-0208.1.

Matheou, G., and J. Teixeira, 2019: Sensitivity to physical and numerical aspects of large-eddy simulation of stratocumulus. *Mon. Wea. Rev.*, **147**, 2621–2639, https://doi.org/10.1175/MWR-D-18-0294.1.

McMichael, L. A., D. B. Mechem, S. Wang, Q. Wang, Y. L. Kogan, and J. Teixeira, 2019: Assessing the mechanisms governing the daytime evolution of marine stratocumulus using large-eddy simulation. *Quart. J. Roy. Meteor. Soc.*, **145**, 845–866, https://doi.org/10.1002/qj.3469.

Neale, R. B., and Coauthors, 2010: Description of the NCAR Community Atmosphere Model (CAM 4.0). NCAR Tech. NCAR/TN-485+STR, 212 pp.

Nicholls, S., 1984: The dynamics of stratocumulus: Aircraft observations and comparisons with a mixed layer model. *Quart. J. Roy. Meteor. Soc.*, **110**, 783–820, https://doi.org/10.1002/qj.49711046603.

Pedruzo-Bagazgoitia, X., and Coauthors, 2020: The diurnal stratocumulus-to-cumulus transition over land in southern West Africa. *Atmos. Chem. Phys.*, **20**, 2735–2754, https://doi.org/10.5194/acp-20-2735-2020.

Pelly, J., and S. Belcher, 2001: A mixed-layer model of the well-mixed stratocumulus-topped boundary layer. *Bound.-Layer Meteor.*, **100**, 171–187, https://doi.org/10.1023/A:1019215221726.

Rapp, A. D., 2016: Observational evidence linking precipitation and mesoscale cloud fraction in the southeast Pacific. *Geophys. Res. Lett.*, **43**, 7267–7273, https://doi.org/10.1002/2016GL069906.

Sasamori, T., 1968: The radiative cooling calculation for application to general circulation experiments. *J. Appl. Meteor.*, **7**, 721–729, https://doi.org/10.1175/1520-0450(1968)007<0721:TRCCFA>2.0.CO;2.

Schneider, T., C. M. Kaul, and K. G. Pressel, 2019: Possible climate transitions from breakup of stratocumulus decks under greenhouse warming. *Nat. Geosci.*, **12**, 163–167, https://doi.org/10.1038/s41561-019-0310-1.

Sloan, L. C., and D. Pollard, 1998: Polar stratospheric clouds: A high latitude warming mechanism in an ancient greenhouse world. *Geophys. Res. Lett.*, **25**, 3517–3520, https://doi.org/10.1029/98GL02492.

Stevens, B., W. R. Cotton, G. Feingold, and C.-H. Moeng, 1998: Large-eddy simulations of strongly precipitating, shallow, stratocumulus-topped boundary layers. *J. Atmos. Sci.*, **55**, 3616–3638, https://doi.org/10.1175/1520-0469(1998)055<3616:LESOSP>2.0.CO;2.

Tan, Z., T. Schneider, J. Teixeira, and K. G. Pressel, 2017: Large-eddy simulation of subtropical cloud-topped boundary layers: 2. Cloud response to climate change. *J. Adv. Model. Earth Syst.*, **9**, 19–38, https://doi.org/10.1002/2016MS000804.

Turton, J. D., and S. Nicholls, 1987: A study of the diurnal variation of stratocumulus using a multiple mixed layer model. *Quart. J. Roy. Meteor. Soc.*, **113**, 969–1009, https://doi.org/10.1002/qj.49711347712.

Twomey, S., 1977: The influence of pollution on the shortwave albedo of clouds. *J. Atmos. Sci.*, **34**, 1149–1152, https://doi.org/10.1175/1520-0469(1977)034<1149:TIOPOT>2.0.CO;2.

Uchida, J., C. S. Bretherton, and P. N. Blossey, 2010: The sensitivity of stratocumulus-capped mixed layers to cloud droplet concentration: Do LES and mixed-layer models agree? *Atmos. Chem. Phys.*, **10**, 4097–4109, https://doi.org/10.5194/acp-10-4097-2010.

van der Dussen, J. J., S. R. de Roode, and A. P. Siebesma, 2014: Factors controlling rapid stratocumulus cloud thinning. *J. Atmos. Sci.*, **71**, 655–664, https://doi.org/10.1175/JAS-D-13-0114.1.

Wang, H., and G. Feingold, 2009: Modeling mesoscale cellular structures and drizzle in marine stratocumulus. Part I: Impact of drizzle on the formation and evolution of open cells. *J. Atmos. Sci.*, **66**, 3237–3256, https://doi.org/10.1175/2009JAS3022.1.

Warren, S. G., C. H. Hahn, J. London, R. M. Chervin, and R. L. Jenne, 1988: Global distribution of total cloud cover and cloud types over ocean. NCAR Tech. Note NCAR/TN-317+STR, 42 pp., http://dx.doi.org/10.5065/D6QC01D1.

Wood, R., 2012: Stratocumulus clouds. *Mon. Wea. Rev.*, **140**, 2373–2423, https://doi.org/10.1175/MWR-D-11-00121.1.

Zapata, M. Z., J. R. Norris, and J. Kleissl, 2020: Coastal stratocumulus dissipation dependence on initial conditions and boundary forcings in a mixed-layer model. *J. Atmos. Sci.*, **77**, 2717–2741, https://doi.org/10.1175/JAS-D-19-0254.1.

Zheng, Y., D. Rosenfeld, and Z. Li, 2018: The relationships between cloud top radiative cooling rates, surface latent heat fluxes, and cloud-base heights in marine stratocumulus. *J. Geophys. Res. Atmos.*, **123**, 11 678–11 690, https://doi.org/10.1029/2018JD028579.

Zouzoua, M., and Coauthors, 2021: Breakup of nocturnal low-level stratiform clouds during the southern West African monsoon season. *Atmos. Chem. Phys.*, **21**, 2027–2051, https://doi.org/10.5194/acp-21-2027-2021.